Cohesive zone modeling of anodic dissolution stress corrosion cracking induced by corrosion product films

Cunguang Chen [a]*, Wenwen Wang [b], Zhiliang Zhang [c], Yanjing Su [d] and Alex A. Volinsky [e]

[a] *Institute for Advanced Materials and Technology, University of Science and Technology Beijing, Beijing, P.R. China;*

[b] *School of Mathematics and Physics, University of Science and Technology Beijing, Beijing, P.R. China;*

[c] *Department of Structural Engineering, Norwegian University of Science and Technology (NTNU), Trondheim, Norway;*

[d] *Corrosion and Protection Center, Key Laboratory for Environmental Fracture (MOE), University of Science and Technology Beijing, Beijing, P.R. China;*

[e] *Department of Mechanical Engineering, University of South Florida, Tampa, USA*

*Corresponding author. Email address: cgchen@ustb.edu.cn (Cunguang Chen). Institute for Advanced Materials and Technology, University of Science and Technology Beijing, 30 Xueyuan Road, Haidian District, Beijing 100083, P.R. China

Cohesive zone modeling of anodic dissolution stress corrosion cracking induced by corrosion product films

Abstract

Damage mechanics based on a cohesive zone model was applied to study the anodic dissolution stress corrosion cracking (SCC) in flat and U-shaped edge-notched specimens. The simulation results show that corrosion product films (CPFs) facilitate crack initiation in SCC due to the CPF-induced stress and CPF rupture. In the flat specimen, SCC susceptibility increases with the CPF thickness and CPF Young's modulus, while it decreases with CPF fracture strength. For the U-shaped edge-notched specimen, the normalized threshold stress intensity factor K_{ISCC}/K_{IC} decreases with the CPF thickness and notch depth.

Keywords: FEM; cohesion; corrosion; cracking; films; stress corrosion cracking; corrosion product films.

1. Introduction

Corrosion product films (CPFs), such as passive films, oxide films or de-alloyed layers, usually form on the surfaces of a specimen and/or at the crack tip during anodic dissolution stress corrosion cracking (SCC). A number of experimental results have shown that the CPF plays a critical role in the initiation and propagation of stress corrosion cracks [1-6]. Kermani *et al.* [1] observed that the SCC of α-brass in ammoniacal solution can be arrested by the formation of the tarnish film at the crack tip. The stress is applied to rupture the tarnish film and to maintain it in the ruptured condition, such that the metal/environment reaction causing cracking can proceed. Forty *et al.* [2] studied the fracture mode of a specimen with the tarnish surface layer and correlated the occurrence of a subsequent localized chemical attack when the specimen with cracked tarnish surface was replaced in the solution. By alternatively tarnishing a brass specimen and deforming it under tension, transgranular SCC cracks were observed to propagate into the ductile specimen. Newman *et al*. [3] proposed the film-induced cleavage model based on the observation that a crack originating in the surface layer can penetrate into the underlying

ductile metallic substrate by several micrometers. Zhang *et al.* [4] and Du *et al*. [5] found that hydrogen and pre-strain facilitated anodic dissolution of brass in Mattsson's solution and increased the CPF growth rate, and the CPF-induced stress would ultimately result in an enhancement of CPF rupture and SCC susceptibility. All these results experimentally proved that the formation and rupture of CPF was a prerequisite for the anodic dissolution SCC.

Mechanical properties of the CPF were also considered as a dominant factor of the SCC process. Systematic studies have shown that the CPF can induce tensile stress at the interface between the matrix metal and the CPF during SCC. The CPF-induced stress on the anion concentration [7] and pH value of the solution [8] and the applied potential [9], and hydrogen content in the specimens [10] were in good agreement with the SCC susceptibility under slow strain rate test (SSRT). In other words, under various experimental conditions, larger CPF-induced tensile stress resulted in higher SCC susceptibility. When the CPF-induced stress changes from tensile to zero or compressive under certain circumstances, the SCC ceases [9]. The same behavior was observed in many SCC systems, such as α-Ti in methanol [9], stainless steel in boiling $MgCl_2$ [11], brass and copper in ammoniacal solution [5] and low alloy steel in marine environments [12]. Based on this experimental evidence, many researchers have concluded that the CPF-induced stress plays a crucial role in SCC [7,13].

Several studies have modeled crack initiation with an idealized traction separation law. The cohesive zone model (CZM) represents the behavior of the fracture process zone and describes the relationship between cohesive tractions and separations across the cohesive crack surfaces. To date, the CZM techniques have been developed to simulate the fracture behavior for a wide range of material systems. In fracture modeling, CZM has found wide applications and received a lot of modifications and developments [14-20]. In recent years, CZM techniques have been also applied to simulate crack propagation in hydrogen embrittlement [21-27]. Serebrinsky *et al*. [21] presented the model of hydrogen embrittlement based on the cohesive

law and reproduced experimental trends. Scheider *et al*. [22] studied the effects of hydrogen diffusion on stable crack propagation by using finite element simulations based on the cohesive model for hydrogen-assisted stress corrosion cracking. Olden *et al*. [23] performed diffusion and cohesive zone-based fracture initiation analysis of notched rectangular tensile specimens of 25% Cr stainless steel for hydrogen-induced stress cracking. Alvaro *et al*. [24] performed crack initiation of hydrogen-induced fracture using the same cohesive zone model approach. In this paper, a CZM is developed and employed to investigate the effects of the CPF on crack initiation in anodic dissolution SCC. The effects of the CPF thickness, CPF Young's modulus, and CPF-induced stress on the initiation of the SCC, SCC susceptibility and threshold stress intensity factor are discussed.

2. Material data and CZM procedures

Not annealed copper substrate with Young's modulus E_s = 130 GPa, yield stress σ_{ys} = 350 MPa and a Poisson's ratio of 0.3 was used in this simulation study. The Young's modulus of the elastic CPF varied from $E_f = 0.2E_s$, $0.5E_s$, E_s to $1.5E_s$ and the CPF thicknesses t_f = 0.0005, 0.001, 0.002, 0.006, 0.01 mm was used. To simulate the CPF-induced stress, the CPF was assigned with a positive thermal expansion coefficient, while for the metallic substrate it was assumed to be zero. It should be noted that similar method has been used to introduce the residual stresses induced by elastic anisotropy [28-30] and welding process [31, 32], in which the thermal expansion coefficients had no specific physical meaning. Experimental results have demonstrated that 1 GPa to 1.5 GPa compressive stress could be generated in the tarnish film of copper in ammoniacal solution during SCC [33]. A suitable expansion coefficient was selected to generate the stress in the CPF and the substrate at a unit temperature increment ΔT = 1°C.

Two-dimensional finite element models of flat and U-shaped edge-notched specimens under tension were created. The specimen was loaded by a remote displacement. The cracking was modeled by the CZM in ABAQUS/CAE. The cohesive elements were located in the middle of the model, schematically shown in Figure 1, with a very small initial thickness $T_c = 10^{-5}$ mm. A 2D plane strain model was constructed with the CPE4 and COH2D4 elements. The boundary conditions were as follows:

$$x = l_0,\ u_1 = D,\ u_2 = 0 \tag{1}$$

$$x = 0,\ u_1 = u_2 = 0 \tag{2}$$

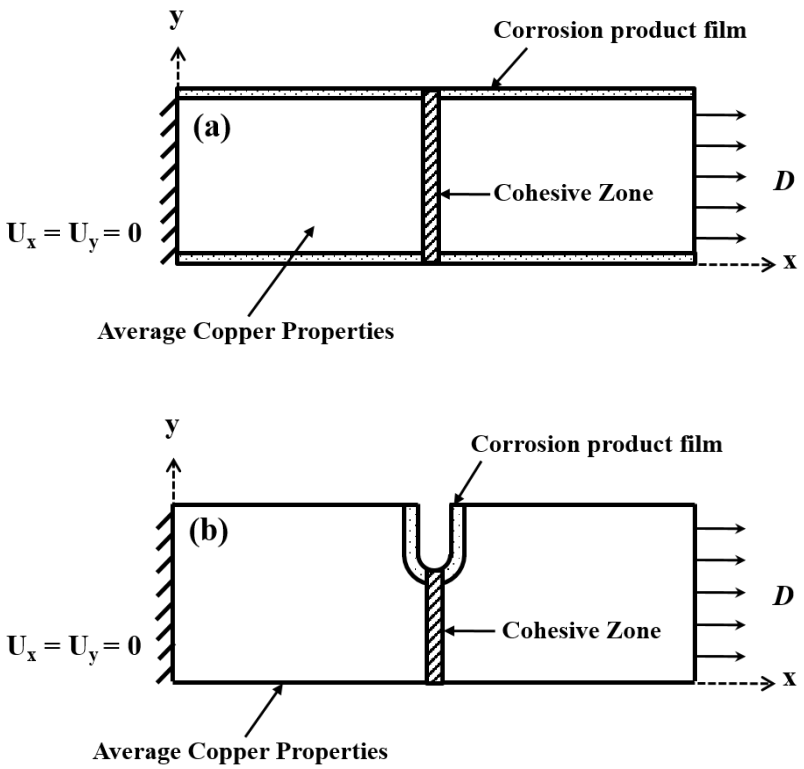

Figure 1. Schematics of the cohesive zone and the boundary conditions. The dimensions of the cohesive zone are exaggerated for clarity: (a) the flat specimen and (b) the U-shaped edge-notched specimen.

The global and local meshes of the U-shaped edge-notched specimen with a CPF are shown in Figure 2. When the notch and CPF dimensions change, the mesh density around the notch is

slightly altered to ensure consistency in the size of the elements created around the notch, which indicates that the meshes created for the cases with different notch sizes will not be completely identical, but should yield similar levels of accuracy.

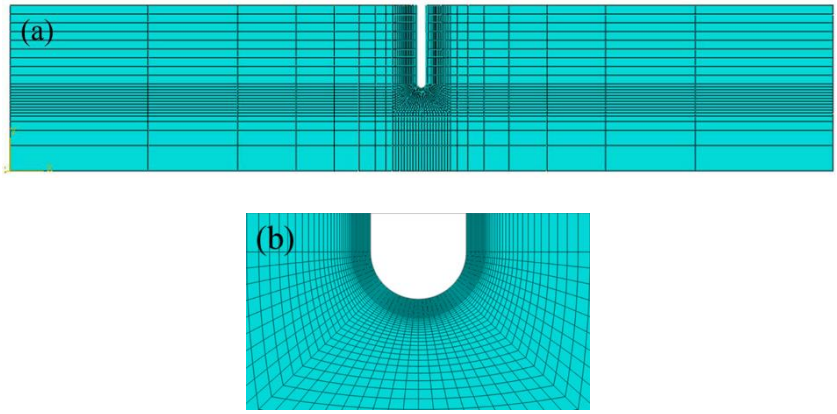

Figure 2. The meshes of the U-shaped edge-notched specimen covered by a CPF: (a) the global and (b) local meshes.

All the micromechanical damage processes that occur within the process zone are embodied in the cohesive zone law. The CZM is characterized by the traction-separation law [34]. The law can be expressed with the crack opening displacement δ and the critical traction σ. The cohesive element behavior is assumed to be linear-elastic initially until the critical traction/displacement has been reached. The triangular cohesive law where the traction after the peak is a decreasing linear function of the opening distance between the upper and lower surfaces of the cohesive elements is commonly used in the literature and available in ABAQUS/CAE and is also employed in the current study, as shown in Figure 3. Crack initiation is defined as the achievement of zero stress and critical opening in the first cohesive element.

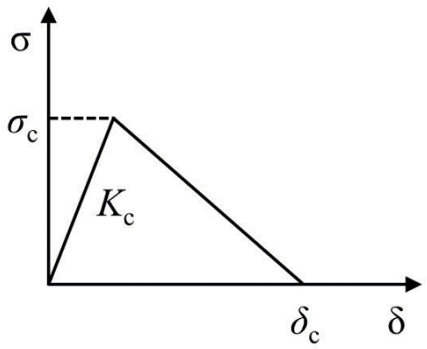

Figure 3. Triangular traction-separation law used in the analysis.

However, the values of these CZM parameters are usually not known and cannot be measured directly from experiments. There are yet no well-established universal rules for determining the values of CZM parameters. The two basic parameters necessary to describe the traction-separation law are the critical traction and the critical separation. The fracture energy is computed by means of the relation $G_c = \frac{K_{IC}^2}{E/_{1-\nu^2}} = \frac{1}{2}\sigma_c\delta_c$ under plane strain, in which K_{IC} of 17 MPa$\sqrt{m}$ [35] is used for copper. After a systematic parameter study, we have chosen a parameter set (σ_c^{sub} = 425 MPa, δ_c^{sub} = 0.00952 mm) for the substrate to ensure that copper tension in the air is controlled the by plastic necking and not by brittle rupture. For σ_c^{sub} < 425 MPa, the cohesive element will cause damage and induce brittle fracture. The fracture strain (or elongation) of copper in the air is taken from our experiments and the value is about 5.38%. For SCC, the fracture behavior is brittle. For the CPF, composed of corrosion porous layer in which the vacancy groups and holes exist, the fracture strength should be lower than the copper substrate. Although the data of the fracture strength of the CPF are not found, a basic value of 300 MPa was used as the critical cohesive traction of the CPF. Other values are discussed in terms of the CPF fracture strength. To make sure that the CPF fails in a brittle manner, the basic value of δ_c^{CPF} = 0.008 mm was chosen as the critical crack opening displacement of the CPF. The sensitivity of simulation results to the chosen value of the CPF cohesive parameter (δ_c^{CPF}) is discussed first. Figure 4 shows the effect of CPF opening displacement δ_c^{CPF} on SCC

susceptibility in a flat specimen with different CPF properties. It can be seen that when the δ_c^{CPF} increases from 0.005 mm to 0.009 mm, the SCC susceptibility (see the definition below) reduces linearly, but only to about 0.15% maximum. In addition, in the analysis with CZM, a large value of the interface stiffness is necessary to assure correct representation of the system behavior before the crack initiation. The stiffness of the cohesive zone, K_c, is chosen as 3.5×10^5 N/mm^3. During the simulation of the cracking by cohesive elements, convergence problem occurs, especially in the model with CPF. A small viscosity v of 10^{-5} in the cohesive law in combination with the use of a small-step increment in the simulations, improves the convergence rate. All the input parameters for the cohesive zone modeling are presented in Table 1 [36].

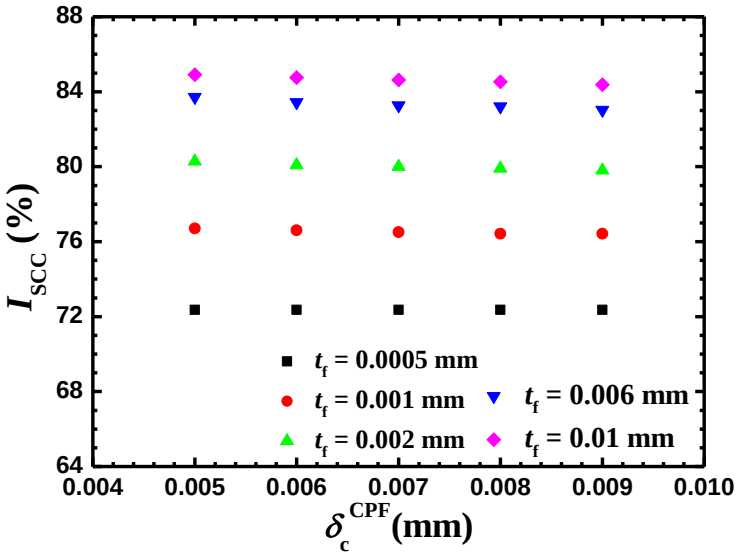

Figure 4. Effect of the critical opening displacement of CPF, δ_c^{CPF}, on the calculated SCC susceptibility based on the cohesive zone modeling with various CPF thickness and E_f/E_s = 0.5, and σ_c^{CPF} = 300 MPa.

Table 1. Input parameters for the cohesive zone modeling [36].

σ_c^{sub}, MPa	δ_c^{sub}, mm	σ_c^{CPF}, MPa	δ_c^{CPF}, mm	K_c, N/mm^3	v, MPa·s
425	0.00953	300 [a]	0.008	3.5×10^5	0.00001

[a] Other values were also employed to discuss the CPF fracture strength.

3. Results and discussion

3.1. SCC susceptibility of the flat specimens

For the flat specimen, SCC susceptibility is defined as $I_{SCC} = (1 - \varepsilon_{\mathrm{FSCC}}/\varepsilon_{\mathrm{F}}) \times 100\%$, where ε_{F} and $\varepsilon_{\mathrm{FSCC}}$ are the fracture strain (or elongation) of the flat specimens in the air and in the solution, respectively. The flat specimen with a CZM covered with a CPF is used to simulate the stress-strain curves of the specimens in solution. $\varepsilon_{\mathrm{FSCC}}$ is estimated from the simulated fracture strain of the flat specimen covered by the CPF. The simulation results of the stress-strain curve of the flat specimen with CPF of various CPF thicknesses, Young's modulus ratio and fracture strength (which is presented by $\sigma_{\mathrm{c}}^{\mathrm{CPF}}$), are shown in Figure 5(a-c), respectively. Figure 5(a) depicts the effects of CPF thickness on the simulated stress-strain curves. It is clearly shown that the yield stress and the fracture strain/elongation decrease with the CPF thickness. Figure 5(b) summarizes the dependence of the fracture strain/elongation on the Young's modulus ratio between the CPF Young's modulus (E_{f}) and the copper substrate Young's modulus (E_{s}). It can be seen that the fracture strain/elongation decrease with the Young's modulus. These results correspond with our previous studies of the CPF-induced stress in flat specimens [32,37]. Tensile CPF-induced stress is generated [33] in the metallic substrate during SCC, and the peak stress localizes at the interface between the CPF and the metallic substrate on the substrate side. The CPF-induced stress increases with the CPF thickness and the CPF Young's modulus [37]. The CPF-induced tensile stress is superimposed on the applied load to deform and fracture the specimens, resulting in the reduction of the yield stress of the substrate (as shown in Figure 5(a)), and the fracture strain (shown in Figure 5(a,b)).

The effect of CPF fracture strength (critical traction $\sigma_{\mathrm{c}}^{\mathrm{CPF}}$) on the stress-strain curve of the flat specimen is shown in Figure 5(c). The fracture strain increases with $\sigma_{\mathrm{c}}^{\mathrm{CPF}}$. The higher

the CPF fracture strength, the harder stress corrosion crack initiation is. Thereby it can be concluded that the high CPF-induced tensile stress and low CPF fracture strength lead to small fracture strain, i.e. high susceptibility to SCC.

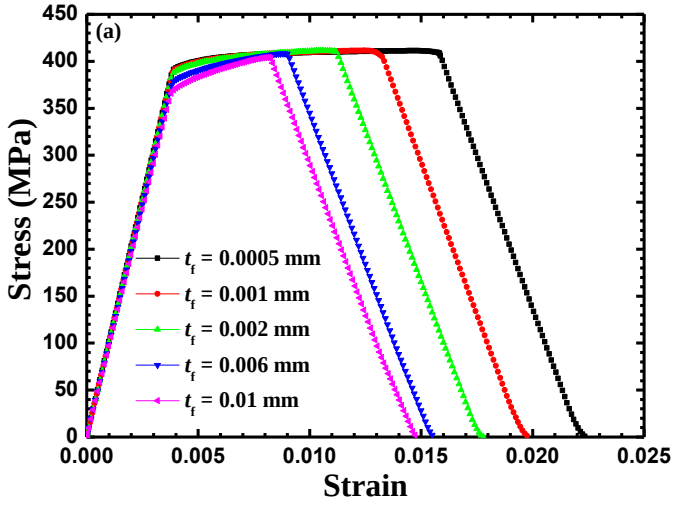

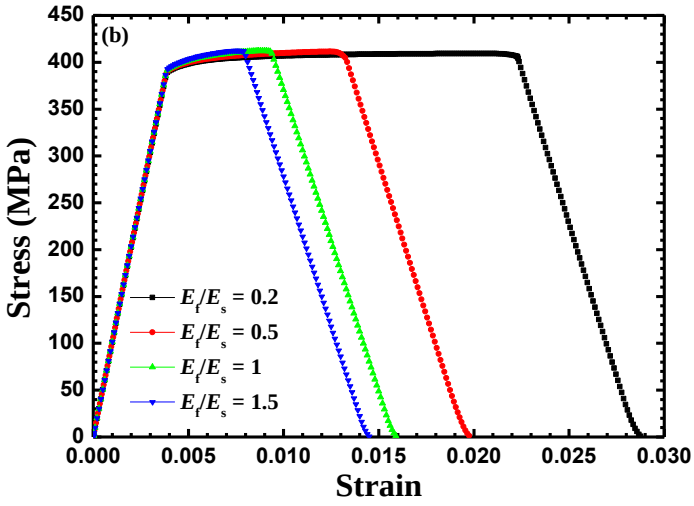

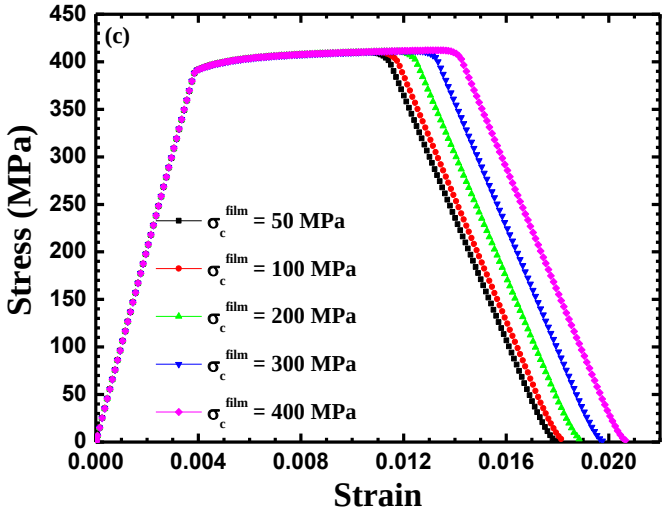

Figure 5. Stress-strain curve obtained from the cohesive zone modeling of the flat specimen with and without CPF with: (a) various CPF thickness and $E_f/E_s = 0.5$, and $\sigma_c^{CPF} = 300$ MPa; (b) various CPF Young's moduli with $t_f = 0.001$ mm and $\sigma_c^{CPF} = 300$ MPa; (c) various CPF fracture strengths with $t_f = 0.001$ mm and $E_f/E_s = 0.5$.

Variations of I_{SCC} calculated based on Fig. 5 for various CPF thickness, Young's modulus ratio E_f/E_s and CPF fracture strength are shown in Figure 6(a,b), respectively. With the increase of CPF thickness and CPF Young's modulus, the I_{SCC} increases, while lower CPF fracture strength results in higher I_{SCC}. The CPF fracture strength is more obvious for thicker CPF. From Figure 6, it can be concluded that CPF can reduce the fracture strain/elongation, while thicker and harder CPF result in higher CPF-induced stress, thus the fracture strain/elongation decreases, and SCC susceptibility I_{SCC} increases. All these results clearly show that cracks initiate more easily with CPF in SCC.

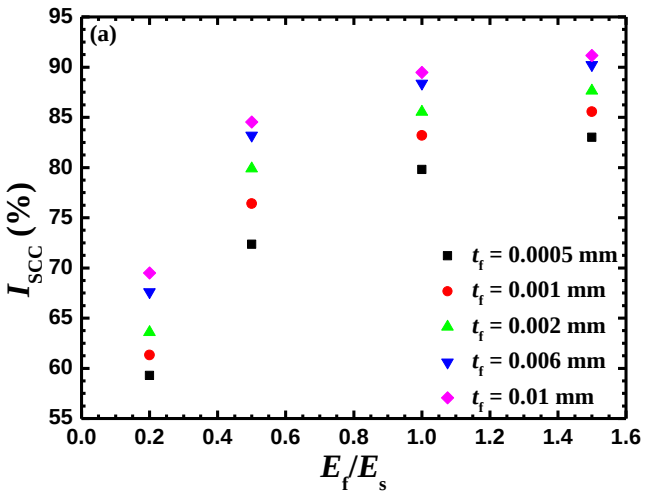

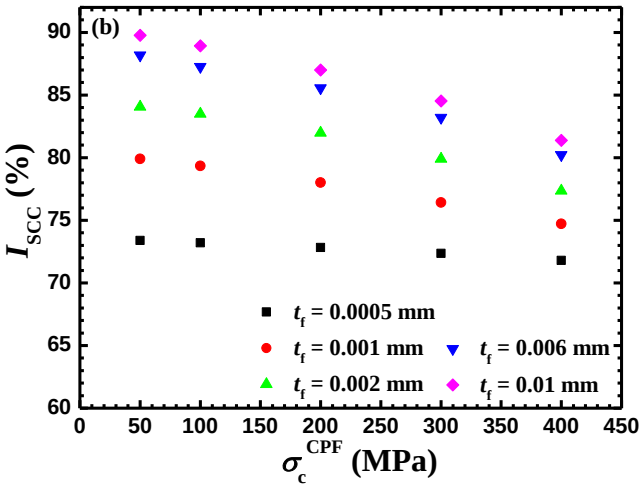

Fig. 6. Calculated SCC susceptibility based on the cohesive zone modeling with: (a) various CPF thickness and Young's modulus ratio E_f/E_s for the CPF with σ_c^{CPF} = 300 MPa, and (b) various CPF fracture strengths of the CPF with Young's modulus ratio E_f/E_s = 0.5.

3.2. SCC susceptibility of the U-shaped edge-notched specimen

For the U-shaped edge-notched specimen, the fracture toughness K_{IC} can be calculated based on $K_{IC} = YP_Q\sqrt{\pi a}/BW$, where $Y = 1.12–0.23(a/w)+10.6(a/w)^2–21.7(a/w)^3+30.4(a/w)^4$, and a, B, W are crack length (or notch depth), specimen thickness and width, and P_Q is the critical load corresponding to the relative crack extension $\Delta a/a$ = 2%. During SSRT in the solution where the CPF forms, the critical stress intensity factor corresponding to SCC extension $\Delta a/a$ = 2% is defined as the threshold stress intensity factor, K_{ISCC}, i.e., $K_{ISCC} = YP_{QSCC}\sqrt{\pi a}/BW$. Lower K_{ISCC} results in easier SCC. The load-displacement curves obtained from the CZM modeling of the U-shaped edge-notched specimen with and without CPF (simulating SCC in the solution) are shown in Figure 7(a). K_{IC} and K_{ISCC} can be calculated based on Figure 7(a). Figure 7(b,c), which show variations of the normalized threshold stress intensity factor K_{ISCC}/K_{IC} with CPF thickness, Young's modulus ratio, and notch depth.

From Figure 7(a), one can calculate P_Q or P_{QSCC} from the intersection of line OP_Q or OP_{QSCC} and the curve in which the slope of the line OP_Q or OP_{QSCC} is 5% less than the elastic

straight line, corresponding to relative crack extension $\Delta a/a$ = 2%. The normalized threshold stress intensity factor K_{ISCC}/K_{IC} shown in Figure 7(b,c) can be obtained based on Figure 7(a). K_{ISCC}/K_{IC} decreases with the CPF thickness, while it is not a strong function of the Young's modulus of the CPF. This reveals that a thick CPF can increase K_{ISCC} or decreases SCC susceptibility. Thereby large CPF-induced stress leads to small K_{ISCC} and high SCC susceptibility. The effect of notch depth on the normalized K_{ISCC}/K_{IC} is shown in Figure 7(c), where K_{ISCC}/K_{IC} decreases with the notch depth. We can be concluded that the normalized K_{ISCC}/K_{IC} decreases with the notch depth. This means that the crack initiates easier in SCC.

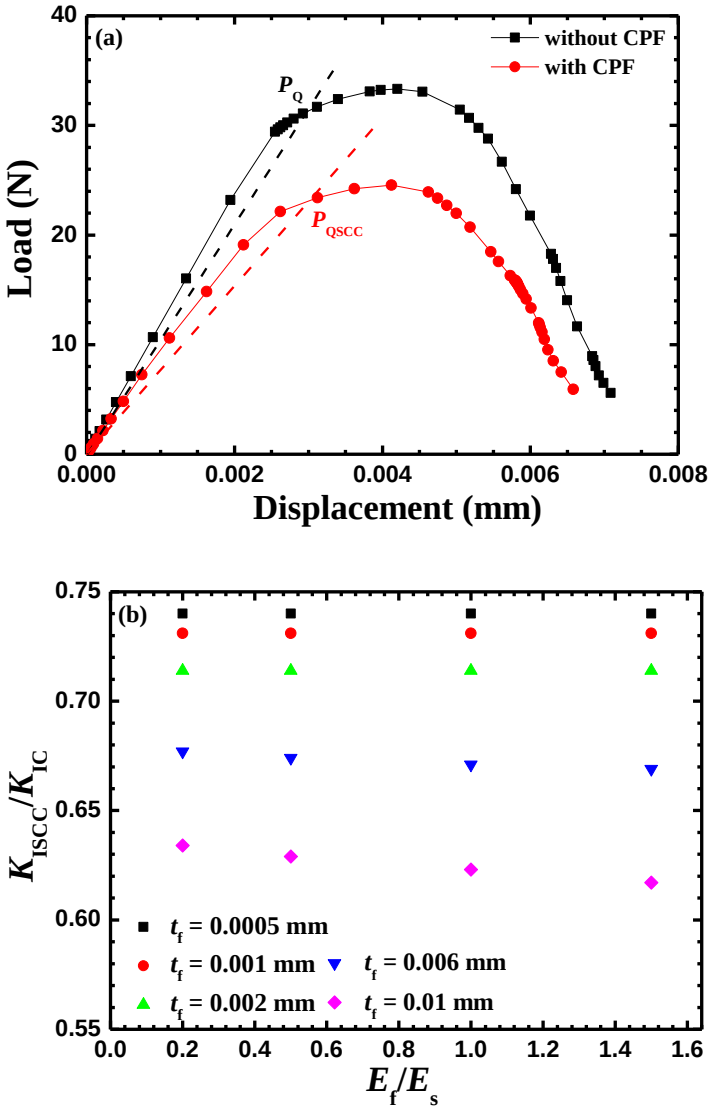

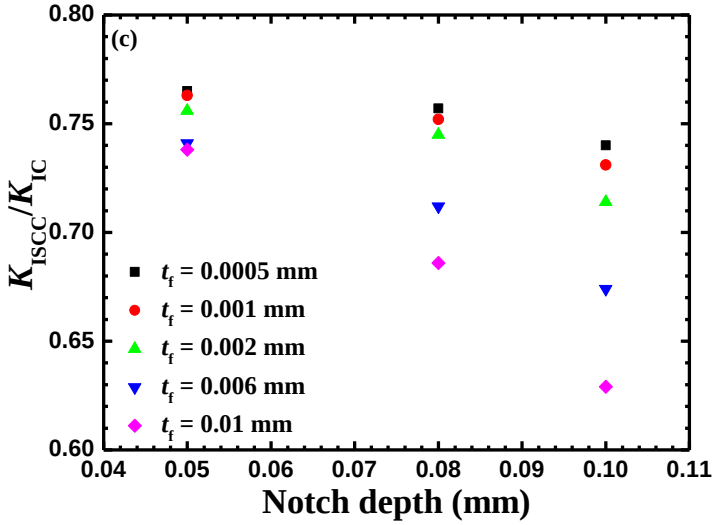

Fig. 7. (a) P_Q and P_{QSCC} in the load-displacement curve of the U-shaped edge-notched specimen, and the variation of the normalized threshold stress intensity factor (K_{ISCC}/K_{IC}) with: (b) various Young's modulus ratio E_f/E_s and CPF thicknesses for the notch depth of 0.1 mm; (c) various notch depths and CPF thicknesses for the CPF Young's modulus ratio E_f/E_s = 0.5.

The fracture in SCC is brittle and the crack usually initiates in the CPF. In the flat and U-shaped edge-notched specimens, the crack initiation occurs first in the CPF. Once the crack initiates, it is equivalent to forming a small notch and leads to a stress concentration in the substrate. It will cause quick fracture of the substrate. Thereby, in the anodic dissolution SCC system, the rupture of the CPF is the dominant factor for SCC. Furthermore, the rupture of the CPF is controlled by the CPF fracture strength. It can be concluded the CPF fracture strength is significant for SCC.

4. Conclusions

A cohesive zone model is developed and applied to anodic dissolution stress corrosion cracking to simulate crack initiation in flat and U-shaped edge-notched specimens. Corrosion product

film facilitates the stress corrosion crack initiation in the flat and U-shaped edge-notched specimens because of the existence of the CPF-induced stress. In the flat specimen, SCC susceptibility I_{SCC} increases with the decrease of the CPF fracture strength and the increase of CPF thickness and CPF Young's modulus. In the U-shaped edge-notched specimen, it is found that the normalized threshold stress intensity factor (K_{ISCC}/K_{IC}) decreases with the CPF thickness and notch depth. Crack initiation occurs first in the CPF and then propagates into the substrate.

Disclosure statement

No potential conflict of interest was reported by the authors.

Funding

This work was supported by the National Natural Science Foundation of China (51571028). AV acknowledges support from the National Science Foundation (IRES 1358088).

References

[1] M. Kermani, J.C. Scully, *The effect of strain-rate upon stress corrosion crack velocity in α-brass in ammoniacal solutions*, Corros. Sci. 19 (1979), pp. 89-95, 97-110.

[2] A.J. Forty, P. Humble, *The influence of surface tarnish on the stress corrosion of α-brass*, Philos. Mag. 8 (1963), pp. 247-264.

[3] R.C. Newman, T. Shahrabi, K. Sieradzki, *Film-induced cleavage of alpha-brass*, Scripta Metall. 23 (1989), pp. 71-74.

[4] C. Zhang, Y.J. Su, L.J. Qiao, W.Y. Chu, *Study on the role of tarnishing film in stress-corrosion cracking of brass in Mattsson's solution*, J. Mater. Res. 25 (2010), pp. 991-998.

[5] X.S. Du, Y.J. Su, C. Zhang, J.X. Li, L.J. Qiao, W.Y. Chu, W.G. Chen, Q.S. Zhang, D.X. Liu, *Pre-strain enhances film rupture to promote SCC of brass in Mattsson's solution-A proposal for a film-rupture-induced SCC mechanism*, Corros. Sci. 69 (2013), pp. 302-310.

[6] M.G. Alvarez, P. Lapitz, S.A. Fernández, J.R. Galvele, *Passivity breakdown and stress corrosion cracking of α-brass in sodium nitrite solutions*, Corros. Sci. 47 (2005), pp. 1643-1652.

[7] X.S. Du, Y.J. Su, J.X. Li, L.J. Qiao, W.Y. Chu, *Inhibitive effects and mechanism of phosphates on the stress corrosion cracking of brass in ammonia solutions*, Corros. Sci. 60 (2012), pp. 69-75.

[8] X.J. Guo, K.W. Gao, L.J. Qiao, W.Y. Chu, *The correspondence between susceptibility to SCC of brass and corrosion-induced tensile stress with various pH values*, Corros. Sci. 44 (2002), pp. 2367-2378.

[9] X.Z. Guo, K.W. Gao, W.Y. Chu, L.J. Qiao, *Correlation between passive film-induced stress and stress corrosion cracking of α-Ti in a methanol solution at various potentials*, Mater. Sci. Eng. A 346 (2003), pp. 1-7.

[10] X.Z. Guo, K.W. Gao, L.J. Qiao, W.Y. Chu, *Stress corrosion cracking relation with dezincification layer-induced stress*, Metall. Mater. Trans. A 32 (2001), pp. 1309-1312.

[11] J.X. Li, W.Y. Chu, Y.B. Wang, L.J. Qiao, *In situ TEM study of stress corrosion cracking of austenitic stainless steel*, Corros. Sci. 45 (2003), pp. 1355-1365.

[12] X.S. Du, Y.J. Su, J.X. Li, L.J. Qiao, W.Y. Chu, *Stress corrosion cracking of A537 steel in simulated marine environments*, Corros. Sci. 65 (2012), pp. 278-287.

[13] R. Nishimura, *Characterization and perspective of stress corrosion cracking of austenitic stainless steels (type 304 and type 316) in acid solutions using constant load method*, Corros. Sci. 49 (2007), pp. 81-91.

[14] H.B. Chew, *Cohesive zone laws for fatigue crack growth: Numerical field projection of*

the micromechanical damage process in an elasto-plastic medium, Int. J. Solids. Struct. 51 (2014), pp. 1410–1420.

[15] X. Chen, X.M. Deng, M.A. Sutton, P. Zavattieri, *An inverse analysis of cohesive zone model parameter values for ductile crack growth simulations*, Int. J. of Mech. Sci. 79 (2014), pp. 206-215.

[16] Y.J. Xu, H. Yuan, *Applications of normal stress dominated cohesive zone models for mixed-mode crack simulation based on extended finite element methods*, Eng. Fract. Mech. 78 (2011), pp. 544-558.

[17] J.H. Lee, Y.F. Gao, K.E. Johanns, G.M. Pharr, *Cohesive interface simulations of indentation cracking as a fracture toughness measurement method for brittle materials*, Acta Mater. 60 (2012), pp. 5448-5467.

[18] F. Moroni, A. Pirondi, *A procedure for the simulation of fatigue crack growth in adhesively bonded joints based on a cohesive zone model and various mixed-mode propagation criteria*, Eng. Fract. Mech. 89 (2012), pp. 129-138.

[19] B. Paliwal, M. Cherkaoui, *An improved atomistic simulation based mixed-mode cohesive zone law considering non-planar crack growth*, Int. J. Solids. Struct. 50 (2013), pp. 3346-3360.

[20] B. Yang, S. Mall, K. Ravi-Chandar, *A cohesive zone model for fatigue crack growth in quasibrittle materials*, Int. J. Solids. Struct. 38 (2001), pp. 3927-3944.

[21] S. Serebrinsky, E.A. Carter, M. Ortiz, *A quantum-mechanically informed continuum model of hydrogen embrittlement*, J. Mech. Phys. Solids 52 (2004), pp. 2403-2430.

[22] I. Scheider, M. Pfuff, W. Dietzel, *Simulation of hydrogen assisted stress corrosion cracking using the cohesive model*, Eng. Fract. Mech. 75 (2008), pp. 4283-4291.

[23] V. Olden, C. Thaulow, R. Johnsen, E. Østby, *Cohesive zone modeling of hydrogen-induced stress cracking in 25% Cr duplex stainless steel*, Scripta Mater. 57 (2007), pp. 615-

618.

[24] A. Alvaro, V. Olden, O.M. Akselsen, *3D cohesive modelling of hydrogen embrittlement in the heat affected zone of an X70 pipeline steel*, Int. J. Hydrogen Energy, 38 (2013), pp. 7539-7549.

[25] N.R. Raykar, S.K. Maiti, R.K. Singh Raman, *Modelling of mode-I stable crack growth under hydrogen assisted stress corrosion cracking*, Eng. Fract. Mech. 78 (2011), pp. 3153-3165.

[26] S. Guzmán, J.C. Gálvez, J.M. Sancho, *Modelling of corrosion-induced cover cracking in reinforced concrete by an embedded cohesive crack finite element*, Eng. Fract. Mech. 93 (2012), pp. 92-107.

[27] H.Y. Yu, J.S. Olsen, A. Alvaro, V. Olden, J.Y. He, Z.L. Zhang, *A uniform hydrogen degradation law for high strength steels*, Eng. Frac. Mech. 157(2016), pp. 56-71.

[28] M. Pezzotta, Z.L. Zhang, M. Jensen, T. Grande, M.-A. Einarsrud, *Cohesive zone modeling of grain boundary microcracking induced by thermal anisotropy in titanium diboride ceramics*, Comp. Mater. Sci. 43 (2008), pp. 440–449.

[29] M. Pezzotta, Z.L. Zhang, *Effect of thermal mismatch induced residual stresses on grain boundary microcracking of titanium diboride ceramics*, J. Mater. Sci. 45 (2010), pp. 382–391.

[30] M.S. Jensen, M. Pezzotta, Z.L. Zhang, M.-A. Einarsrud, T.Grande, *Degradation of TiB_2 ceramics in liquid aluminum*, J. Eur. Ceram. Soc. 28 (2008), pp. 3155–3164.

[31] X.B. Ren, Z.L. Zhang, B. Nyhus, *Effect of residual stresses on the crack-tip constraint in a modified boundary layer model*, Int. J. Solids Struct. 46 (2009), pp. 2629-2641.

[32] X.B. Ren, Z.L. Zhang, B. Nyhus, *Effect of residual stresses on ductile crack growth resistance*, Eng. Fract. Mech. 77 (2010), pp. 1325-1337.

[33] W.J. Yuan, Z.L. Zhang, Y.J. Su, L.J. Qiao, W.Y. Chu, *A novel method to measure the*

residual stress in a corrosion film formed on metallic substrates, Corros. Sci. 68 (2013), pp. 128-133

[34] V. Tvergaard, J.W. Hutchinson, *The relation between crack growth resistance and fracture process parameters in elastic-plastic solids*, J. Mech. Phys. Solids. 40 (1992), pp. 1377-1397.

[35] E.W. Qin, L. Lu, N.R. Tao, J. Tan, K. Lu, *Enhanced fracture toughness and strength in bulk nanocrystalline Cu with nanoscale twin bundles*, Acta Mater. 57 (2009), pp. 6215-6225.

[36] Y.F. Gao, A.F. Brower, *A simple technique for avoiding convergence problems in finite element simulations of crack nucleation and growth on cohesive interfaces*, Modell. Simul. Mater. Sci. Eng. 12 (2004), pp. 453-463.

[37] W.W. Wang, Z.L. Zhang, X.C. Ren, Y.J. Guan, Y.J. Su, *Corrosion product film-induced stress facilitates stress corrosion cracking*, Sci. Rep. 5 (2015), pp. 10579.